



Contents lists available at ScienceDirect

Cement and Concrete Research

journal homepage: www.elsevier.com/locate/cemconres

3D-printable engineered cementitious composites (3DP-ECC): Fresh and hardened properties

Kequan Yu^a, Wes McGee^b, Tsz Yan Ng^b, He Zhu^b, Victor C. Li^{b,*}

^a Tongji University, College of Civil Engineering, Shanghai, 200092, China

^b University of Michigan, Ann Arbor, MI 48109, USA

ARTICLE INFO

Keywords:

3D printing
Self-reinforced
Engineered cementitious composite
Rheology
Mechanical properties

ABSTRACT

3D printing (3DP) is an emerging digital construction method for concrete materials. A major impediment to efficient 3D concrete printing (3DCP) is the need for steel reinforcement, the placement of which is incompatible with the 3DP process. Unlike plain concrete, ductile self-reinforced engineered cementitious composite (ECC) holds promise to remove the dependence on steel reinforcement. The objective of this research is to develop a 3D-printable ECC (3DP-ECC). The fresh rheological and hardened mechanical properties of 3DP-ECC are investigated. The robotically printed tensile specimens demonstrated the familiar multiple microcracking and strain-hardening behavior of conventionally cast ECC. Significant orthotropy is revealed in the compressive properties. The interface between printed layers is found to be toughened by a printed groove-tongue joint. The developed 3DP-ECC was used to print a twisted column with 150 layers, reaching a height of 1.5 m. This research lays the groundwork for efficient robotically 3D-printed structures of complex shapes.

1. Introduction

Extrusion-based 3D concrete printing (3DCP) is a digital construction method developed in recent decades [1], attracting worldwide attention in industry [2] and academy [3,4]. Through a fully digital process of 3DCP, construction time could be significantly reduced, while the construction quality could be improved, leading to an increase in productivity in the construction sector [5]. 3DCP material and structural elements with complex geometry and hybridized functions including internal curing, self-cleaning, and self-healing properties have been demonstrated [6,7]. Additionally, 3DCP could eliminate formwork which typically accounts for half of the production cost in cast-in-place construction [8,9]. The elimination of formwork also addresses labor shortages and landfill waste challenges.

Despite the advantages of 3DCP, reinforcement (conventionally steel) is necessary to ensure structural load capacity and reliability due to the intrinsic brittleness of concrete material [10,11]. One of the major challenges of 3DP concrete is the inherent incompatibility between the extruded filament layering process and the steel rebar placement process. Although various new reinforcement concepts are being explored [10,12,13], these approaches typically increase the complexity of the printing process and hinder the efficiency of 3DCP.

Engineered cementitious composite (ECC), a strain-hardening fiber-reinforced cementitious material, features high tensile strength and ductility [14]. With the fiber volume no more than 2%, the tensile strength of ECC ranges from 4 to 20 MPa and the tensile strain capacity ranges 3–12% [15]. The tensile ductility of ECC is therefore two to three orders of magnitude higher than that of plain concrete. In a uniaxial direct tensile test, the resulting stress-strain curve of ECC resembles that of ductile steel with a yield point followed by subsequent strain-hardening. The excellent tensile property of ECC provides a plausible solution for 3DP self-reinforced structural element carrying tension without the need for steel reinforcement [16]. Previous research demonstrated good seismic resistance of a two-story ECC frame building in a shake table test, which highlights the potential of using ECC with reduced or no steel reinforcement in structures [17].

The challenge of meeting the contradicting requirements of pumpability and buildability in 3DCP is magnified by the relatively high fiber content (around 2% by volume) and high aspect ratio (around 300–750) of synthetic fibers in ECC. While studies have been conducted on the development of pumpable 3DP-ECCs, the findings indicate a lack of sufficient buildability resulting in premature collapse failure during layer-by-layer printing process [18–20]. Further, conflicting tensile behaviors of 3DP-ECC have been reported. Some experimental results

* Corresponding author.

E-mail address: vcli@umich.edu (V.C. Li).

demonstrate that the tensile properties, including the tensile strength and ductility of printed ECC, are comparable or higher than those of cast ECC, which is attributed to the enhanced fiber alignment during mixture delivery and filament extrusion processes [16,18,19]. However, inferior tensile properties compared to those of cast ECC have also been reported, possibly a result of different material composition, delivery and extrusion systems [20]. A 3DP-ECC with robust pumpability, buildability, and tensile properties remains to be developed.

Previous research [21–23] demonstrated that the mechanical performance of the interfaces between printed layers is strongly influenced by material composition, print time interval, surface moisture, physical layer interlock, and extrusion speed. However, the systematic characterization of interface toughness has not been conducted. The layer interfaces may also influence the compressive properties, leading to an orthotropic compressive strength and stress-strain relationship in the parallel and perpendicular directions to the print direction. While anisotropic compressive strength [24–26] has been reported, the constitutive stress-strain relationships in the longitudinal and transverse directions (with respect to the print direction) needed for the structural design of 3DP-ECC elements has not been studied.

The objective of this research is to develop a 3DP-ECC with desirable flowability and buildability through proper tuning of rheological properties to match the customized pumping and extrusion equipment [27]. The tensile properties and size effect of robotically printed dog-bone specimens are determined from uniaxial tension tests. Interfacial fracture toughness is measured using three-point bending tests on specimens with smooth and grooved surface treatments to verify their corresponding influence. Anisotropic compressive strength and stress-strain relationship are determined using printed cube and prism specimens. The digital image correlation (DIC) method is used to capture the complete compression damage process.

2. Experimental preparation

2.1. Raw materials and mix proportions

The 3DP-ECC consists of four parts, i.e., the binder materials, the fine sand, the reinforcing fiber, and the chemical additives. The binder materials are ordinary Portland cement (OPC) 52.5R and fly ash (FA). The chemical compositions of OPC and FA are shown in Table 1. F75 silica sand with particle size ranging from 50 to 550 μm is used as the fine aggregate. Polyvinyl alcohol (PVA) fiber with 1.2% oil (by mass) is used as the reinforcement. The physical and mechanical properties of PVA fiber are listed in Table 2. A polycarboxylate-based high range water reducer (HRWR) is used for quick liquefaction of dry powder, and powder-based hydroxypropyl methylcellulose (HPMC) is added to control the viscosity and cohesion of the mixture. The average particle size and viscosity value of HPMC are 75 μm and 7500–14,000 mPa.s (2% aqueous solution at 20 °C), respectively.

The mix proportion of 3DP-ECC is listed in Table 3. High-volume fly ash (mass ratio of FA/OPC = 3.3) is used to partially replace the amount of cement, which, on the one hand, reduces the viscosity and consequently increases the flowability and pumpability of 3DP-ECC; on the other hand, moderates the environmental impact of 3DP-ECC. The sand/binder and water/binder ratios are 0.26 and 0.24, respectively. 2% PVA fiber by volume is added to ensure a strain-hardening behavior of 3DP-ECC.

Table 1
Chemical compositions of cement and fly ash.

	SiO ₂	CaO	Al ₂ O ₃	Fe ₂ O ₃	MgO	Na ₂ O	K ₂ O	SO ₃	TiO ₂	L.O.I. (950 °C)
OPC	20.10	62.92	5.62	2.17	1.14	0.30	0.85	2.92	–	3.84
FA	46.84	20.86	15.49	6.95	2.66	1.00	2.76	2.05	0.77	7.41

Table 2
Properties of PVA fibers.

Fiber parameters	Diameter d_f , μm	Length L_f , mm	Tensile strength, MPa	Elastic modulus, GPa
Value	39	8	1600	30

Table 3
Mix proportion of 3DP-ECC.

Cement (kg/m ³)	Fly ash (kg/m ³)	Silica sand (kg/m ³)	SP (kg/m ³)	VMA (kg/m ³)	Water (kg/m ³)	PVA fiber (kg/m ³)
309	1026	345	3	2	321	26

2.2. Printing setup and mixing process

The robotic 3DP setup used in this research is developed to maximize geometric control while addressing the challenges and opportunities for printing with ECC [27]. It includes two parts, the feeding, and extruding systems (Fig. 1). The feeding system consists of a hopper mounted to a servo-driven peristaltic pump, which feeds a 4 m hose connected to a custom-built servo-driven progressive cavity (PC) pump that is mounted at the end of the robotic arm. The peristaltic pump has the capability for handling a high-viscosity mixture but also has the disadvantage of significant pulsation, though this can be mitigated with pulsation dampeners. Its relatively open flow design improves the passage of fiber-reinforced ECC through the pump. The peristaltic pump, without the need for disassembly after use, is easier to clean and flush than other pump types.

The extruding system is based on a 6-axis industrial robot with a 2.8 m reach and 120 kg payload, mounted to a linear gantry (Fig. 1). A pressure transducer at the inlet of the PC pump provides feedback to the peristaltic pump to maintain a constant inlet pressure, even as the PC pump starts/stops or varies flow. Due to the pulsation inherent in peristaltic pumps and the deadtime between the pump and the transducer, the current setup causes a significant pressure swing, which can exceed the pressure-holding ability of the single-stage PC extruder and lead to excess material in the nozzle. By modifying the nozzle geometry to create an open area in the front face, these material pulses can be buffered and shaped as they exit the nozzle. Additionally, for ECC mixtures, the rotator/stator in the PC pump requires a much larger size to minimize the interaction or pinching that occurs between the fibers (even with soft PVA fibers) and the rotator/stator. This pinching leads to higher friction/rotor torque which could result in catastrophic damage to the PC pump and low tensile performance of 3DP-ECC due to its undesirable fiber dispersion. While friction can be reduced by lowering the mix viscosity, it is also observed that a minimum viscosity is critical to preventing bleeding.

The printing process is shown in Fig. 1(b), the ECC material is transferred from the mixer to the peristaltic pump and the extruder to build the printing item.

Small scale mixing (15–25 L) was employed in the present research considering the time-dependent fresh properties of ECC and the amount of ingredient materials required. The mixture was carefully prepared to ensure a superior fiber dispersion for optimal material and printing performance. All the dry ingredients including powder-based HPMC were initially mixed for 30 s at the speed of 90 rpm. Water and HRWR were then added and agitated for another 2 min at the speed of 180 rpm

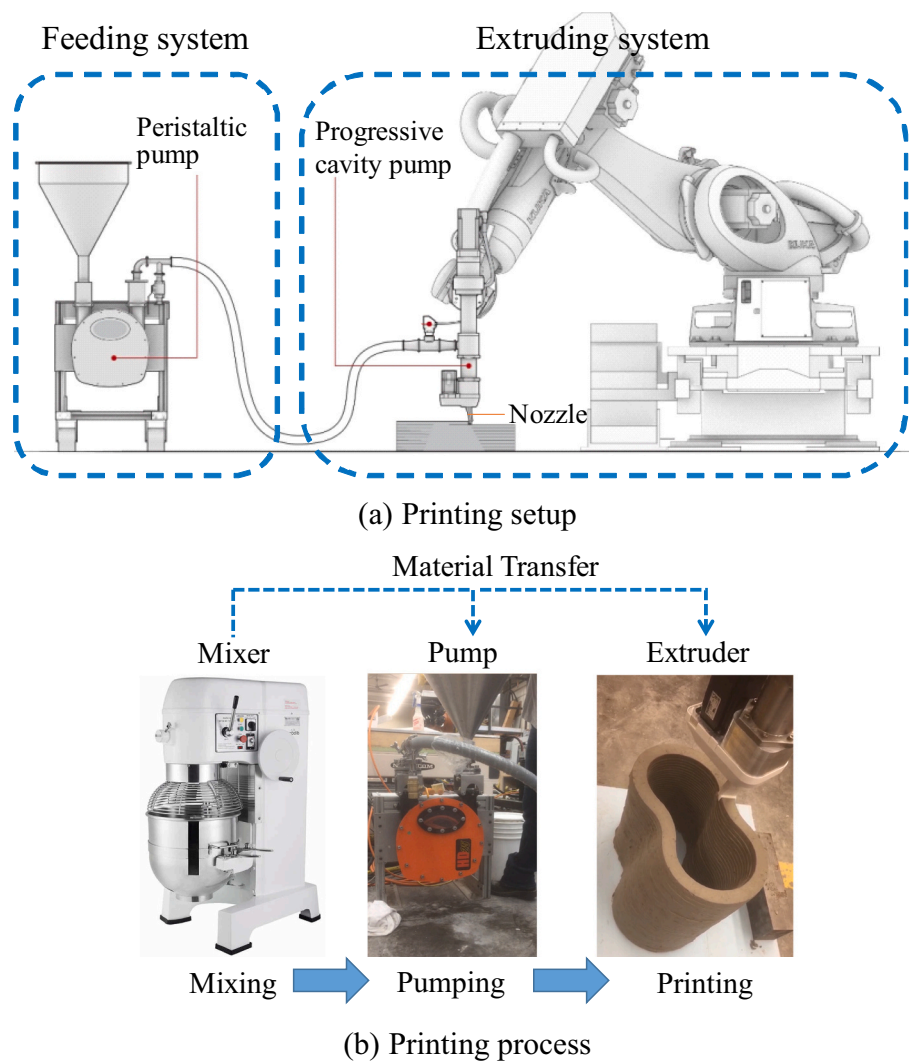


Fig. 1. Printing equipment and process.

to swiftly liquefy the dry particles. PVA fibers were added into the matrix in two parts and mixed at the speed of 180 rpm for 2 min. After all the fibers were blended, mixing continued for an extra 2 min. This prepared mixture was partly used for 3D printing. Material from the same mix batch was also used to cast specimens to compare property differences resulting from two different material processing methods.

2.3. Test preparation of 3DP-ECC in the fresh state

The challenges of balancing the time-dependent rheological properties of flowability and buildability in 3DCP have been widely recognized. The demands for ideal rheological properties are different for the mixing, transport, extrusion, and placement phases of 3DP-ECC. In each phase, complex interactions between equipment, process, and material take place [28].

The fine-tuned rheological properties of fresh ECC are essential for its application in 3D printing. The rheological behaviors of 3DP-ECC determine not only the pumpability and extrudability [29–31], and the deformation stability of the placed filaments (buildability), but also the interlayer bond property that affects the performance of the printed ECC structure in the hardened state. The addition of 2% fiber by volume significantly impacts the rheological characteristics of ECC. Moreover, high fiber volume and high fly ash content have secondary impacts on the pumping system. While the addition of fly ash is known to increase the flowability of ECC, excess increases can cause bleeding during the

feeding and extruding process. This effect, coupled with high fiber volume fraction, risks segregation and blockage of flow in the system. Therefore, a balanced combination of flowability and buildability of 3DP-ECC with an appropriate open time is targeted in the present research.

Three types of fresh-property tests were conducted in this research program: The flow-table test, the shape-retention test, and the green-strength test.

The flow-table test was conducted to determine the flowability of the fresh ECC mixtures from 20 (hereafter set as T_{20}) to 100 min (T_{100}) after water addition at intervals of 20 min (Fig. 2a) as per ASTM C1437 [32]. The fresh ECC was filled into an inverted half cone with diameters of 70 mm and 100 mm at top and base, respectively, and height of 60 mm. After removal of the cone and after 25 shocks (table-drops), the diameter of the spread material on the flow-table was measured to determine the open time of proper flowability for the current printing system.

The buildability or the shape-retention ability of mixed ECC, reflecting the ability to bear the self-weight of consecutive layers while limiting its deformation, was determined following the procedure described in [33]. The fresh ECC at T_{20} was filled into a cone. After cone removal, a 600 g weight was placed on the top surface of the ECC and the deformation at the base circle was measured after 1 min [33]. The smaller the spread diameter, the higher the buildability of the mixture. The test setup is shown in Fig. 2b.

The green strength-deformation relationship of the fresh 3DP-ECC at

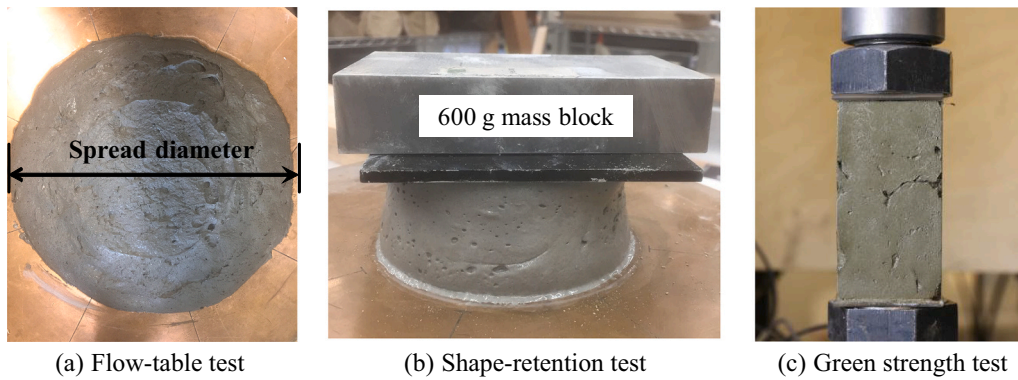


Fig. 2. Fresh test setups.

T_{20} , which provides a general guideline for the upper limit printing speed, was obtained from the prism ($50 \times 50 \times 100$ mm) compression test. The green prism deformation was measured using the digital image correlation (DIC) method [34,35]. Randomly black-white speckles were sprayed onto the specimen surface for deformation calculation. A digital camera with a resolution of 6000×4000 pixels was used to automatically take pictures at intervals of 5 s. The compression test setup is shown in Fig. 2c and loading rate was 3 mm/min to ensure test completion in 10 min to minimize any buildability increase during the test.

2.4. Test preparation of 3DP-ECC in the hardened state

2.4.1. Compressive test

Due to the presence of the layer interface, the compressive properties of hardened 3DP-ECC, including the compressive strength and stress-strain relationship, are expected to differ with the loading directions, i.e., perpendicular and parallel to the interfacial/printing direction (Fig. 3a). It is expected that the specimens tested parallel to the printing direction will show inferior properties due to the lack of fiber-bridging effect in the layer interface. Therefore, the compressive properties in both directions were investigated and compared to the properties of cast ECC specimens.

The compressive strength of 3DP-ECC was obtained from cube specimens with 50 mm edge length and the stress-strain relationship was obtained from prism specimens. The cross-section of printed ECC filament for the compression test was 50 mm in width and 10 mm in thickness by employing a print nozzle with a cross-section of 50×10 mm. The nozzle motion speed was 50 mm/s and the extrusion speed was 1.5 L/min. Both the cube and prism specimens were cut from a printed wall, as shown in Fig. 3b. Four curing ages, namely 1d, 3d, 7d, and 28d were chosen to obtain the strength development of 3DP-ECC. At each curing age, four cube specimens and three prism specimens were

prepared. The specimens are named Cube/Prism-Per/Par-A, where Per/Par is the abbreviation of perpendicular or parallel to the printing direction, and A is the curing age. For comparison, cast ECC cube and prism specimens were prepared for 28d testing. The compressive test plan is detailed in Table 4.

The test setups of both cube and prism specimens are shown in Fig. 4 and the loading rate of both tests was fixed at 0.5 mm/min until failure. The crack formation of the prism specimen was monitored by the DIC method. Digital images were automatically taken at intervals of 20 s.

2.4.2. Uniaxial tensile test

For cast ECC, plain dogbone specimens (Fig. 5a) according to JSCE specification [36] were prepared in this study to measure the stress-strain behavior under uniaxial tension. The cross-section of the tensile specimen was $30 \text{ mm} \times 13 \text{ mm}$ and the gauge length was 80 mm. For printed ECC, a filament with the same cross-section ($30 \text{ mm} \times 13 \text{ mm}$) was first printed in the mold using a print nozzle with a cross-section of 30×13 mm. The nozzle motion and extrusion speeds were 50 mm/s and 1.2 L/min, respectively. The rest of the mold was then filled with cast ECC to form the dogbone shape (Fig. 5b). The dogbone geometry ensures the occurrence of microcracks in the narrow-gauge region. Both cast and

Table 4

Compressive test matrix of 3DP-ECC specimens.

Curing age	1d	3d	7d	28d
Specimen				
Cube-Per	4	4	4	4
Cube-Par	4	4	4	4
Prism-Per	3	3	3	3
Prism-Par	3	3	3	3
Cast-cube	-	-	-	4
Cast-prism	-	-	-	3

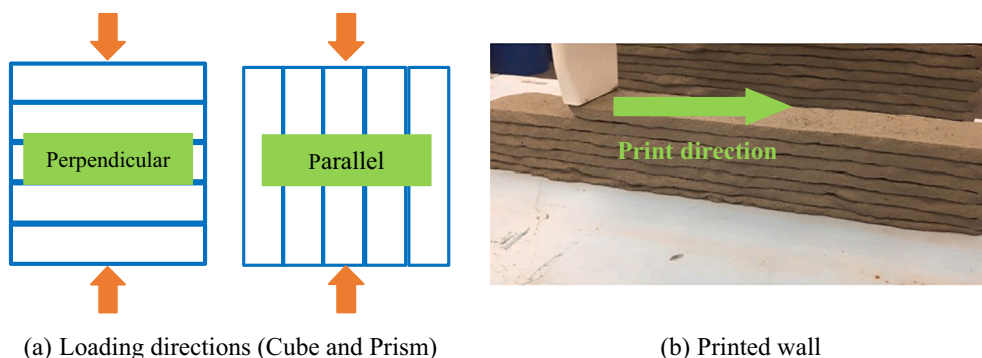


Fig. 3. Loading directions of 3DP-ECC specimens.

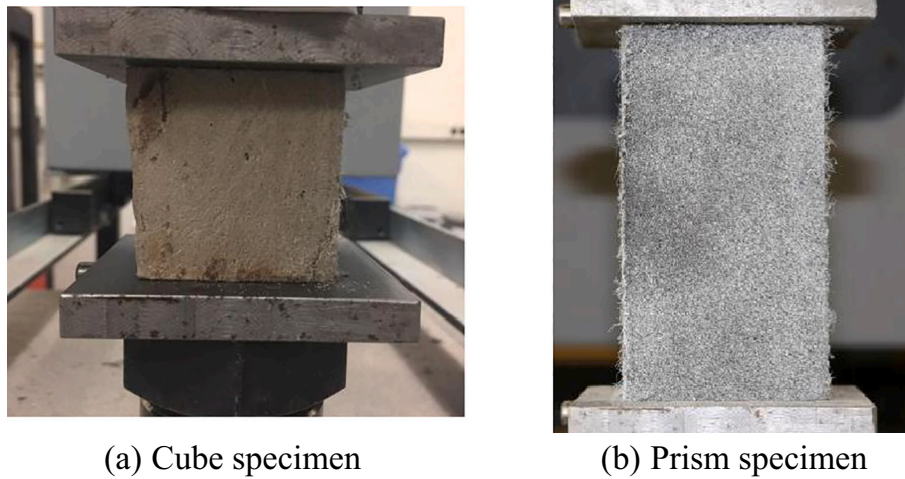


Fig. 4. Compressive test setup of 3DP-ECC.

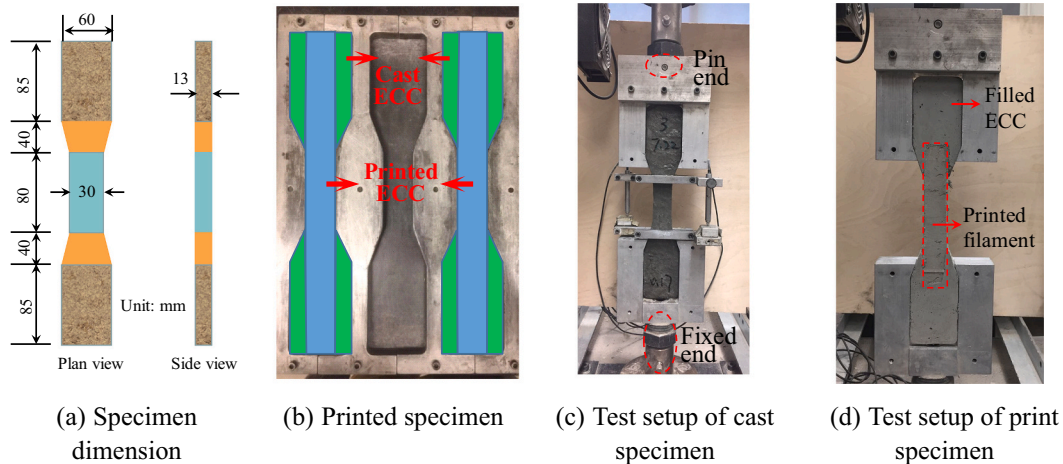


Fig. 5. Tensile specimen and test setup.

printed ECC specimens were prepared and tested to obtain their tensile properties at 3d and 28d. The size effect of printed and cast ECC on tensile properties was also investigated by comparing the tensile performance with different layers or thicknesses. The printed specimen was named as P-xL-yd, where x means the number of layers, y means the curing age (3d or 28d); while the cast specimen was named as C-x-yd, where x means the thickness of the specimen (13 and 26 mm), y means the curing age. At least three samples were prepared for each case.

The uniaxial tensile test setups of the cast and printed specimens are shown in Fig. 5c-d. A fixed-pin end connection was used at the end of the steel grip to minimize bending stress induced by potential eccentricity or misalignment. The tensile tests were conducted at a fixed loading rate of 0.5 mm/min according to JSCE [36]. Two linear variable displacement transducers (LVDTs) fixed on an aluminum frame was used to measure the elongation of the specimens. The average reading of the two LVDTs was adopted to calculate the tensile strain. The load value was read from the load-cell of the test machine.

2.4.3. Interfacial fracture test

The mechanical property of the interface between adjacent filaments of 3DP-ECC has not previously been investigated. In this study, the interfacial fracture behavior of printed ECC was determined by the three-point bending test with a single notch in the center of the specimen (Fig. 6a, b). The specimen length was 180 mm with a span of 160 mm cut

from a printed wall (Fig. 6c, d); the specimen height and thickness were 40 mm and 30 mm, respectively. The notch/depth ratio was 0.35 [37]. The specimen was cut from the printed wall with the layer thickness of 10 mm. The cross-section of the print nozzle is 30×10 mm and the nozzle motion speed was 50 mm/s, leading to an extrusion speed of 0.9 L/min. The fracture property of the printed ECC itself was also determined to further evaluate the weakness of the layer interface. The intra-layer notched beam was prepared with the same dimensions as the inter-layer notched beam (Fig. 6b) but with the notch located inside one of the layers.

Additionally, different surface treatments, i.e., smooth (Fig. 7a) and grooved (Fig. 7b) surfaces of 3DP-ECC were used to investigate their influence on the interfacial fracture toughness. It is known that physical interlocking between adjacent layers would increase the mechanical strength of the printed mortar [21]. The interlocking in 3DP-ECC was achieved by grooving the filament using a corrugated extrusion nozzle [38]. The placement of the next extruded filament on the grooved surface resulted in groove-and-tongue joints. The groove depth and width in the present research were approximately $3 \text{ mm} \times 3 \text{ mm}$. At least four specimens were prepared for each case. The specimens were named Inter(Intra)-S(G)-xd, where Inter and Intra are the abbreviations of inter-layer and intra-layer, S and G represent the smooth and grooved surfaces, x means the curing age. The detailed fracture property test plan is shown in Table 5.

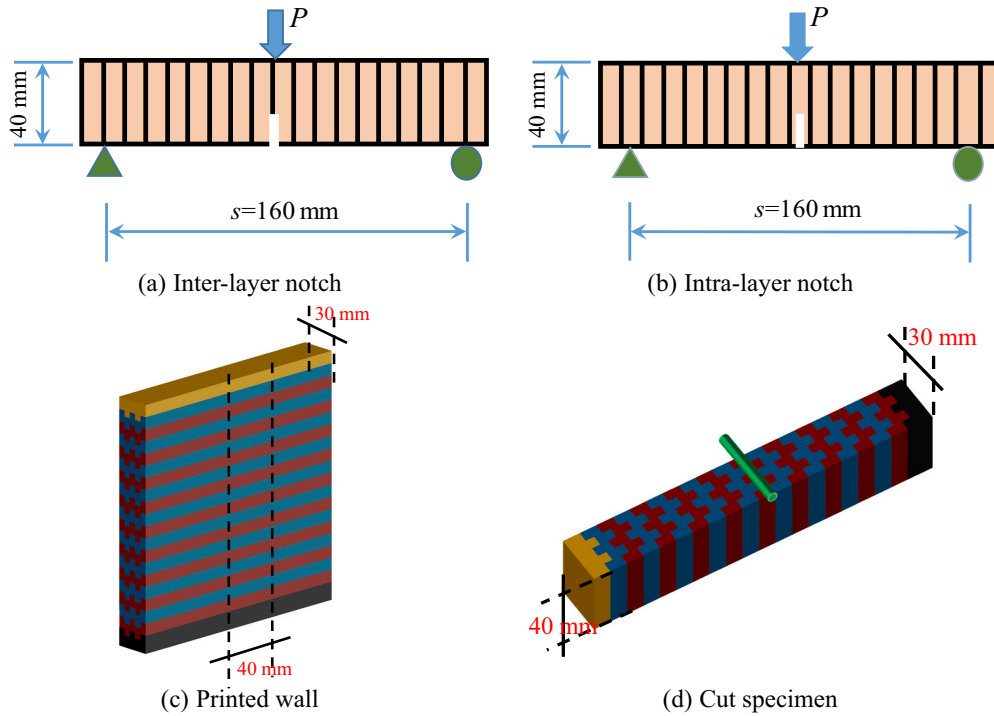


Fig. 6. Geometry of three-point bending specimen [38].

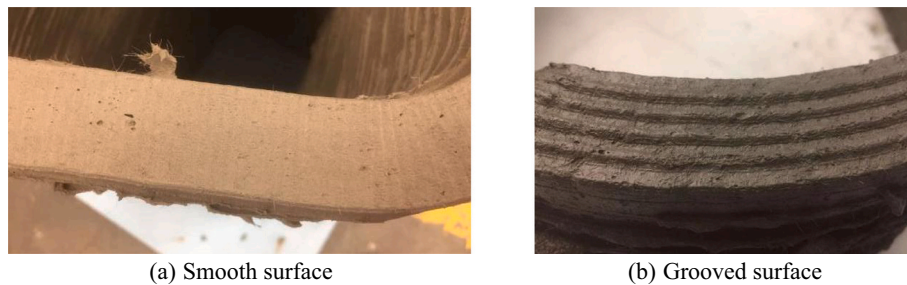


Fig. 7. Surface treatments of print specimen [38].

Table 5
Interfacial fracture properties test plan of 3DP-ECC.

Surface treatment	Smooth	Grooved
Notch location		
Inter-layer	1d, 3d, 7d, and 28d	1d, 3d, 7d, and 28d
Intra-layer	1d, 3d, 7d, and 28d	-

3. Results and discussion

3.1. Rheological properties of fresh ECC

3.1.1. Flowability and shape retention

The spread diameters of the fresh ECC mixtures from T_{20} to T_{100} at 20-min intervals were measured in the flow-table test (Fig. 2a). As shown in Fig. 8a, the spread flow decreased with rest time (measured as time elapse after water addition in the mixing process) as expected. It is noted that the mixture did not exhibit flow before the flow table drop was applied. This behavior implies an almost zero-slump state, benefiting the shape-retention ability of fresh ECC. The mixture at T_{80} was found to be difficult to pump in the current peristaltic pumping system. To balance viability for pumping with reasonable shape-

retention, the minimum spread diameter of fresh ECC was determined to be 120 mm.

From the shape-retention test (Fig. 2b), the spread diameters of the fresh ECC under a static 600 g weight were measured at different rest times (Fig. 8b). Similar to the flowability test results, the spread diameter in the shape-retention test also decreased with rest time, reflecting an increasing shape-retention ability and buildability.

The combination of flowability and shape-retention tests determines the open time of the present printable ECC to be around 70 min after water addition to enable an appropriate balance between pumpability and buildability. Using an ECC mix at T_{20} , both pumpability and buildability were demonstrated with a 1.5 m high 3DP-ECC twisted column with 150 printed layers of 10 mm thick per layer (Fig. 8c) [38].

3.1.2. Green compressive stress-deformation relationship

Material parameters including rheology, green strength, and stiffness have a significant influence on the printing parameters, such as layer height limit and print speed [40]. Till now, the literature on the early-age material properties of 3DP-ECC is basically non-existent. In the present research, a pilot study on the green compressive stress-deformation relationship of 3DP-ECC was conducted (Fig. 2c). The deformation of fresh 3DP-ECC at T_{20} , which could provide a deformation-based failure criterion for printed ECC element, was

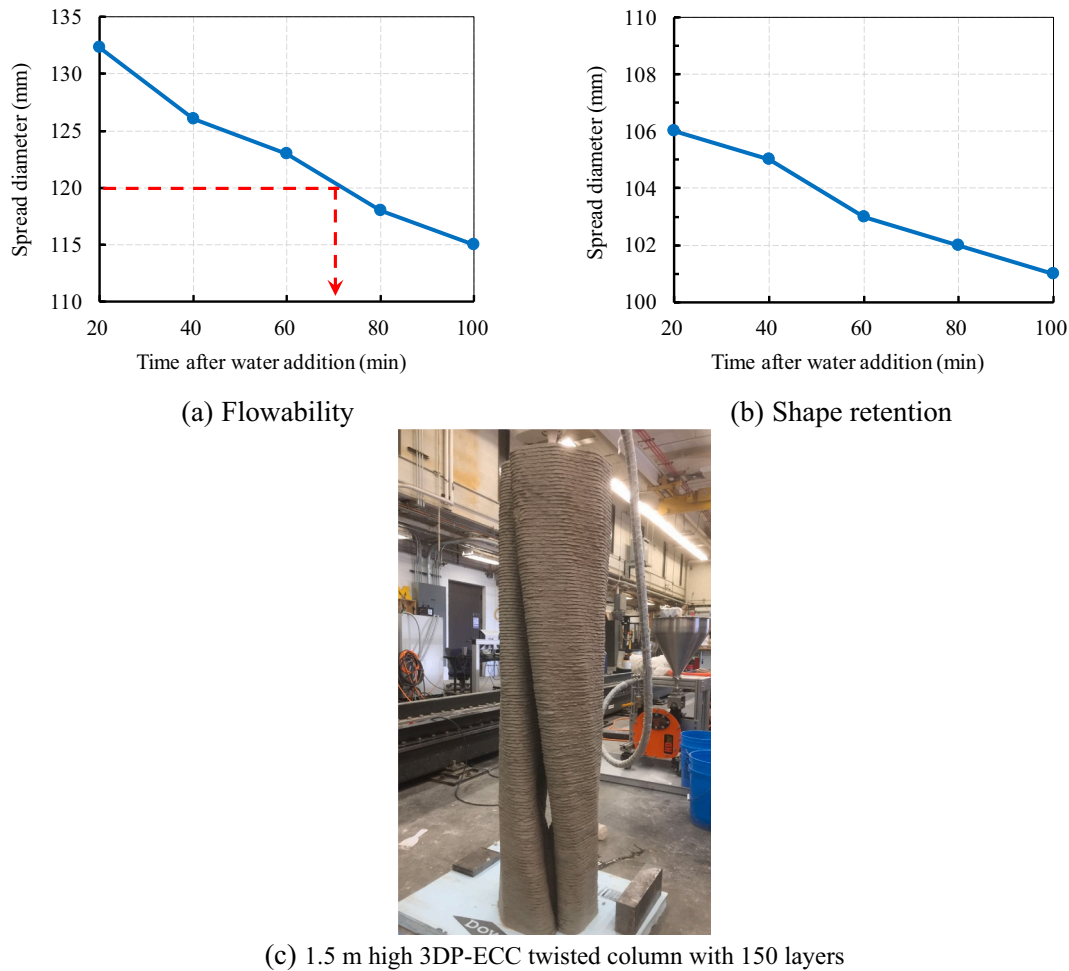


Fig. 8. Rheological properties of fresh ECC.

monitored by the DIC method.

The fresh prism experienced shortening with barreling of the center portion under increasing load (Fig. 9a) [40]. The displacement field in the X-direction (when Y-axial strain is 10%) deduced from the DIC data is shown in Fig. 9b. The positive number in the scale bar (Unit: mm) means the same direction as the X-axis. The prism experiences generally symmetrical but significant expansion at the lower central portion of the specimen. The compressive stress increased monotonically even under a large Y-axial deformation exceeding 20% (Fig. 9c). The Young's modulus ($E = 0.14$ MPa) of fresh 3DP-ECC could be calculated from the slope of the initial segment of the stress-strain curves at compressive stress below 2 kPa.

The upper limit of the printing speed could be estimated from the stress-strain curves. For instance, when the 10% compressive strain (1 mm deformation of a 10 mm-thick printed filament) is set as the target (allowable) deformation, 6.0 kPa compressive stress could be applied to the filament according to the stress-strain relationship. The loading speed in the present test is 3 mm/min and the deformation target is 10 mm ($10\% \times 100 \text{ mm} = 10 \text{ mm}$), indicating that the 6 kPa should be applied within 3–4 min, setting a ceiling for the printing speed to prevent material failure [38]. Moreover, the upper limit of printing speed varies from project to project and should be determined by comprehensively consider the following factors: the print system, the print material property and the print scheme. The print system includes feeding and extruding capacity. The material property includes material printability and its variation with time and curing conditions. The print scheme includes the print sequence, filament dimensions and print scale. The upper limit of print speed is highly important to judge the system's

competitiveness and needs further investigation.

3.2. Compressive property of hardened 3DP-ECC

3.2.1. Strength development with curing age

The compressive strength development of cube and prism specimens in two directions, namely perpendicular and parallel to layer interface, from 1d to 28d are summarized in Fig. 10. For cube specimens (Fig. 10a), both Cube-Per and Cube-Par increased steadily with curing age, the compressive strengths of Cube-Per-1d, and Cube-Par-1d were 50% of the values at 28d; while the corresponding strength ratios of Cube-Per-7d and Cube-Par-7d were approximately 90%. The compressive strengths of Cube-Par at all the curing ages were only 75% of those values of Cube-Per, which was closely related to the failure modes of these two kinds of cube specimens (Fig. 11a-b). The compressive strength of the cast cube specimen was 31.20 MPa at 28d, close to the value of Cube-Per-28d (30.60 MPa), implying, as expected, that the layer interface did not notably influence the compressive strength when the loading direction was perpendicular to the layer interface.

The prism specimens (Fig. 10b) shared a similar trend to that of cube specimens with curing age and the strength ratios of Prism-Per to Prism-Par also stabilized around 0.75. The compressive strength of Prism-Per-28d was 28.15 MPa at 28d, comparable to the value of cast specimen at 29.80 MPa. It was also observed that the parallel specimens (cube and prism) had larger error bars or variability in most cases than those of perpendicular specimens, which could be attributed to the more brittle failure mode of parallel specimens.

Fig. 11 illustrates the failure modes of cube and prism specimens,

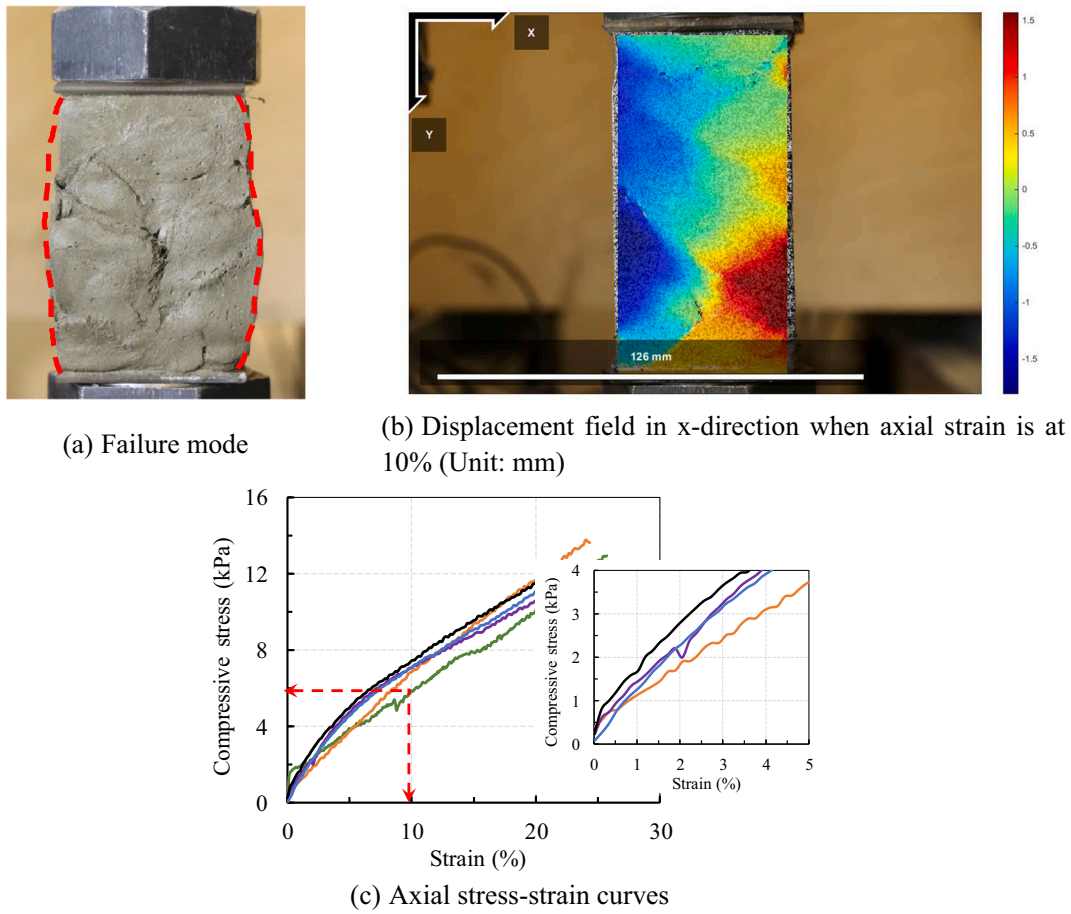


Fig. 9. Green property of fresh ECC at T_{20} .

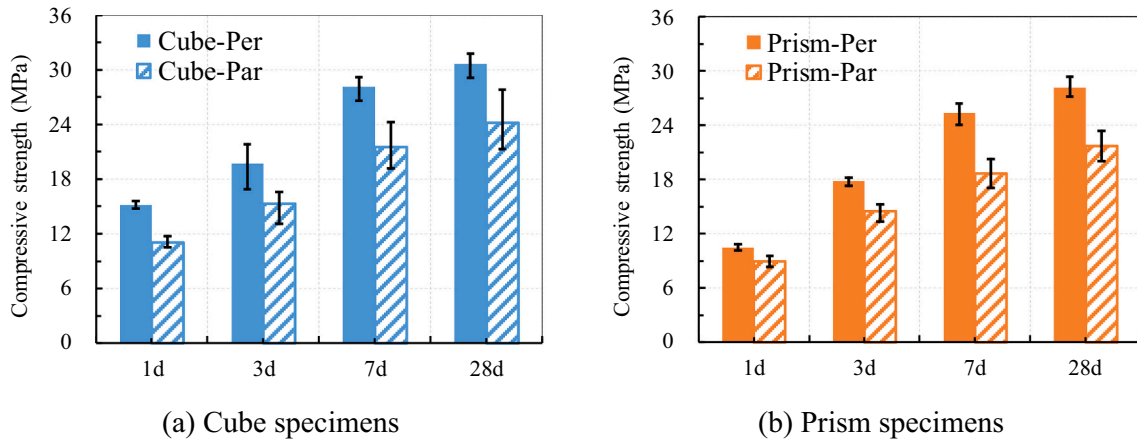


Fig. 10. Compressive strength development.

which shows the influence of the loading direction. The Cube-Per and Prism-Per specimens shared a similar failure mode and crack pattern to those of cast specimens with substantial multiple cracking accompanying the main crack and experienced a significant amount of deformation before failure (Fig. 11a, c) [41]. Although there was negligible fiber-bridging between the layer interfaces, the fiber-bridging effect inside the filament remains effective in resisting crack propagation of Cube-Per and Prism-Per specimens under loads.

In contrast, the failure modes of Cube-Par and Prism-Par specimens were notably different with only a few cracks. The main crack (Cube-

Par) or the initial crack (Prism-Par) penetrated through the layer interface, resulting in a relatively brittle failure mode, with relatively smaller deformation and lower compressive strength (Fig. 11b, d). No buckling failure of individually printed filament under compression was observed in the Prism-Par specimen. The adjacent filament may have acted as lateral support.

The compressive strength ratios between cube and prism specimens (both perpendicular and parallel specimens) were approximately 0.9 (Fig. 12), except for the specimens at 1d, which meant that this strength ratio was mainly controlled by the specimen slenderness regardless of

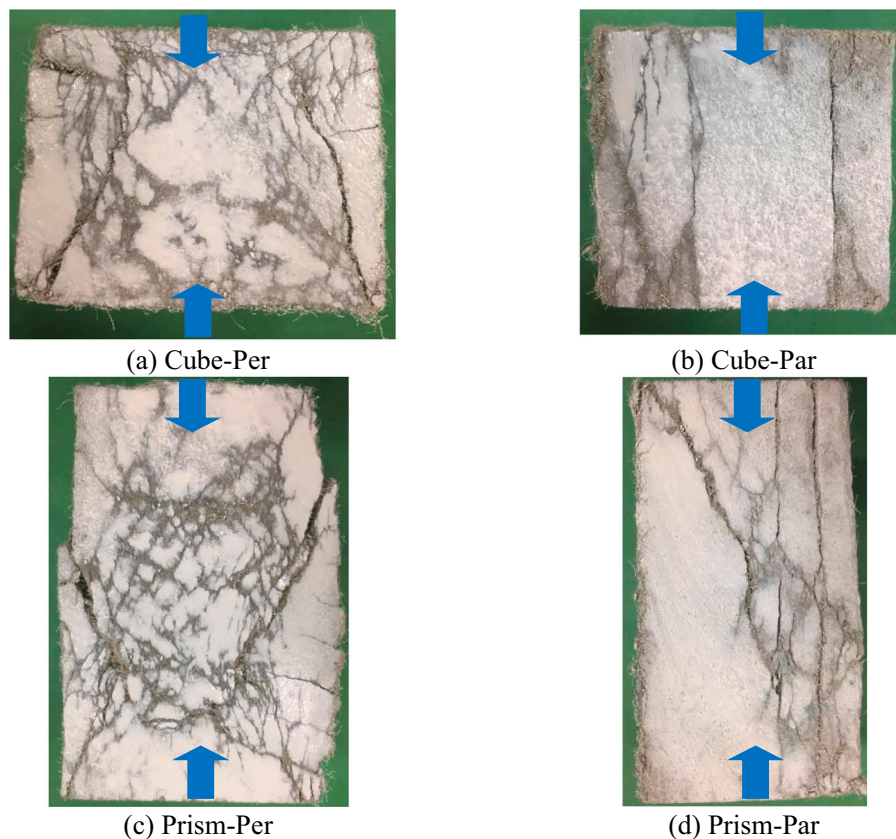


Fig. 11. Failure modes of cube and prism specimens at 28d (blue arrow indicates the loading direction). (For interpretation of the references to colour in this figure legend, the reader is referred to the web version of this article.)

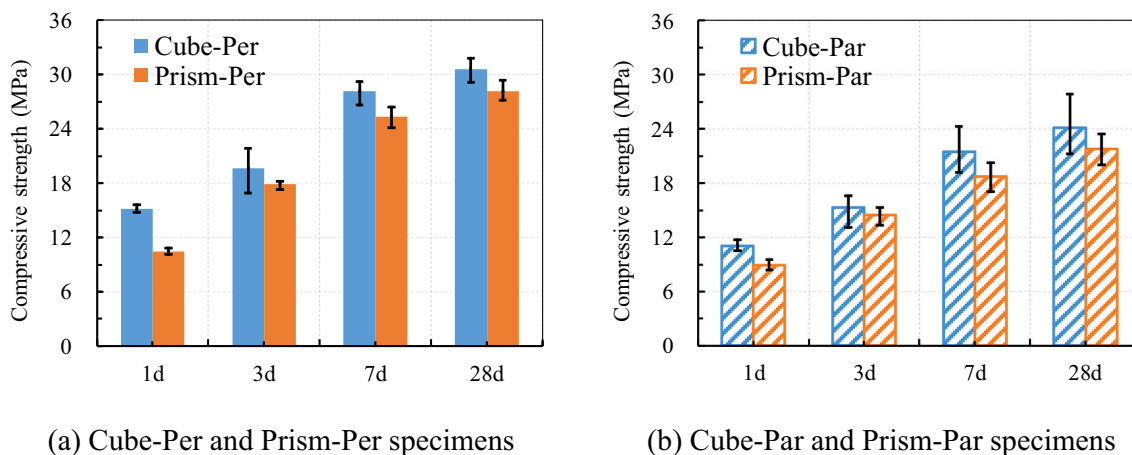


Fig. 12. Compressive strength development of cube and prism specimens.

the loading directions.

3.2.2. Stress-strain behavior

Fig. 13 shows the crack pattern of prism specimens at 28d. Failure of the Prism-Par specimens was initiated with a vertical crack penetrating through the layer interface (Fig. 13a). Only a few cracks could be detected at the final failure stage (Fig. 13b), which resulted in a small deformation of the Prism-Par specimen. The weak interface parallel to the compression load accentuates the splitting failure mode seen in a brittle material.

The Prism-Per specimen, however, developed tortuous crack patterns possibly following the kink-trap mechanism at the layer interface

[42] (Fig. 13c, d). Crack developments are stable with the presence of PVA fibers, promoting more microcracks growth from multiple sites. This results in delayed failure with a higher load and large deformation of Prism-Per specimen from the accumulated damage, consistent with the stress-strain curves shown in Fig. 14.

The compressive stress-(Y-axial) strain behaviors of 3DP-ECC and cast prisms at 28d are displayed in Fig. 14. The axial strain is calculated by displacement values extracted from the DIC images in the center 50 mm length to avoid the influence of lateral restraints at the two loading ends. The mechanical parameters, i.e., Young’s modulus (the slope of the stress-strain curve before 30% of the peak stress), compressive peak stress and corresponding strain were obtained from the stress-strain

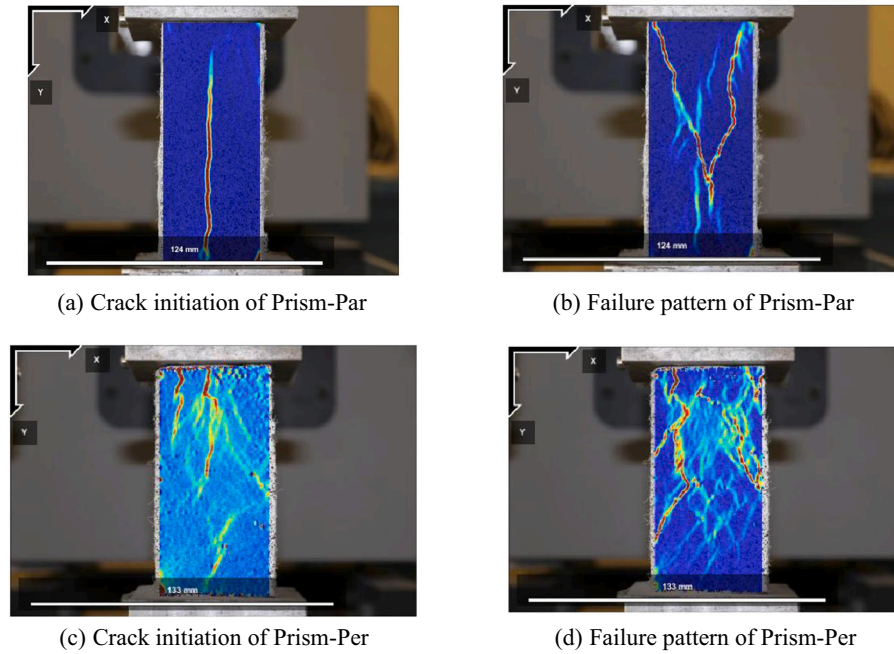


Fig. 13. Crack distribution of prism specimens.

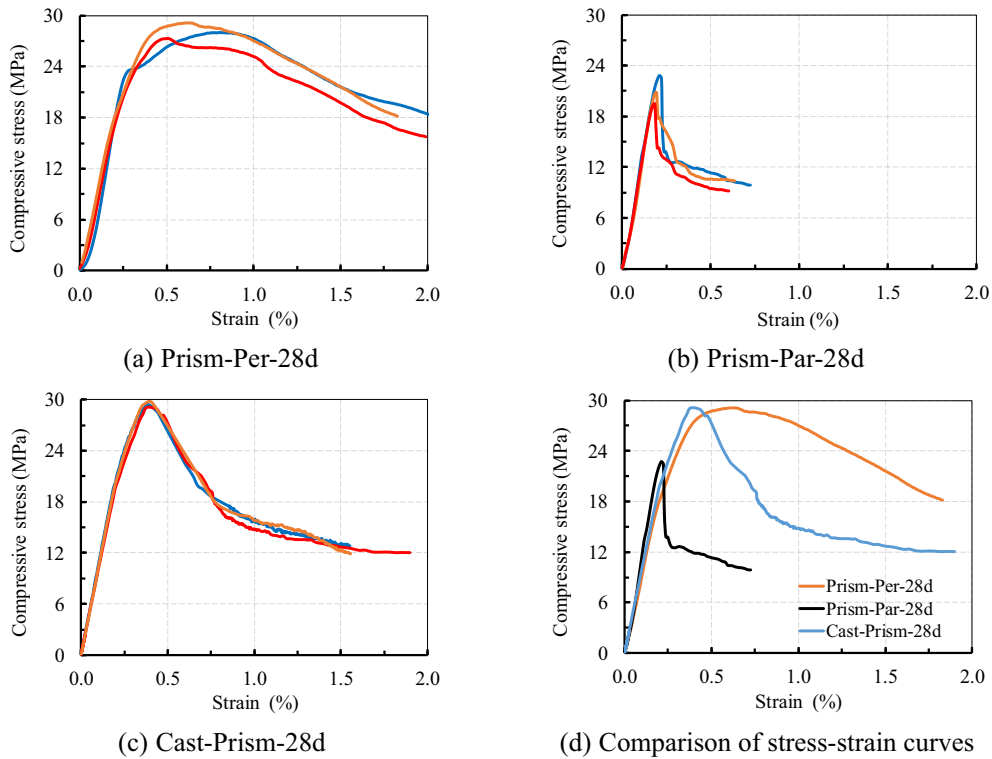


Fig. 14. Compressive stress-(Y-axial) strain curves of the 3DP-ECC prism.

curves.

The Young's modulus of Prism-Per specimen was 10.67 GPa, 16% lower than that of Prism-Par prism (12.71 GPa), and 6% lower than the values obtained from the cast prism (11.27 GPa), which is consistent to the previous research [43,44]. Although the space between two filaments was invisible and considered negligible, the accumulation of the closure of multiple spaces in the prism would add notable deformation to the total deformation, reducing Young's modulus of the Prism-Per

specimen. This phenomenon suggests the need for special consideration when designing the compression zone of 3DP-ECC elements or structures.

The average peak compressive stresses of Prism-Per and Prism-Par were 28.15 and 21.05 MPa, respectively, and their corresponding compressive strains differed significantly with values of 0.65% and 0.20%, respectively (Fig. 14a-b). The compressive strain of Prism-Per was larger than the value of cast ECC (0.39%, Fig. 14c), which could

be attributed to the tortuous crack of Prism-Per specimen and the space between two filaments.

The smaller strain value of the Prism-Par specimen indicated a premature failure, leading to lower compressive strength and steeper descending branch compared to those of Prism-Per specimen specimens (Fig. 14d). The Prism-Per specimen sustains higher post-peak load capacity than that of the cast prism due to tortuous crack following the kink-trap mechanism. The compressive constitutive behavior required careful calibrations for future designs given the vast differences in behavior between the Prism-Per and Prism-Par specimens (Fig. 14d).

3.3. Tensile properties of hardened 3DP-ECC

The tensile stress-strain behaviors of printed and cast ECC specimens with different thicknesses at both 3d and 28d are displayed in Fig. 15. All the specimens demonstrated robust multiple cracking (Fig. 15g-h) and strain-hardening performance with a tensile strain capacity of around 3.0%. There is no reduction in tensile properties in terms of first cracking stress, peak stress and strain capacity of 3DP-ECC specimens from 1 layer to 2 layers (Fig. 15b-c), while the cast ECC with thicker cross-section experienced an apparent reduction in tensile performance due to the size effect (Fig. 15e-f) [45].

The detailed tensile parameters of printed and cast ECC specimens at different curing ages are summarized in Table 6. For printed specimens, the peak stress increased from 2.37 MPa of P-1L-3d to 3.38 MPa of P-1L-28d, while the corresponding strain capacity decreased by 10%. The

Table 6
Tensile parameters of printed and cast ECC.

	First cracking stress (MPa)	Peak stress (MPa)	Strain capacity (%)
P-1L-3d	1.85 (0.09)	2.37 (0.01)	3.43 (0.04)
P-1L-28d	2.86 (0.22)	3.38 (0.03)	3.09 (0.25)
P-2L-28d	2.64 (0.06)	3.34 (0.04)	3.09 (0.03)
C-13-3d	1.63 (0.07)	2.25 (0.04)	3.45 (0.05)
C-13-28d	2.56 (0.04)	3.36 (0.07)	3.00 (0.04)
C-26-28d	1.86 (0.30)	2.91 (0.14)	2.67 (0.02)

Note: number in parentheses is the standard deviation of corresponding parameters.

tensile properties of cast specimens shared a similar tendency with curing ages from 3d to 28d. It was observed that the peak stress and strain capacity of P-2 L-28d were almost equal to the values of P-1L-28d, exhibiting a negligible size effect due to the unchanged fiber dispersion in both 1- and 2-layer specimens. However, the tensile peak stress and strain capacity decreased by 14% and 11%, respectively, when the cast specimen thickness doubled from 13 mm to 26 mm. This is likely due to the change from 2D fiber orientation to 3D, which decreased the crack bridging efficiency and resulting in diminished tensile performance [45].

Moreover, the printed samples exhibited a less pronounced strain hardening (in terms of stress increase per unit strain) than the cast

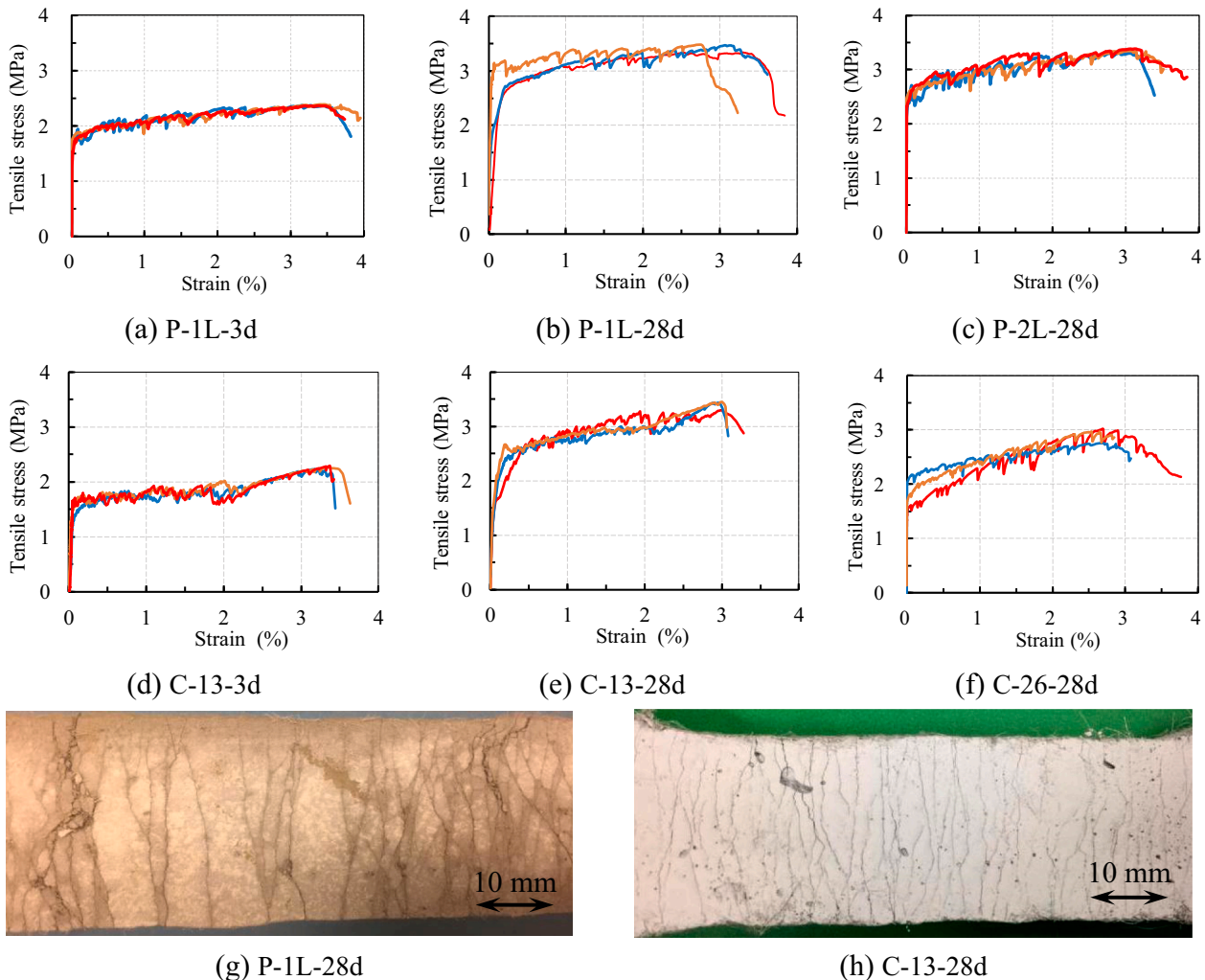


Fig. 15. Tensile stress-strain curves and crack pattern of ECC specimen.

specimens. The ratios of the peak to cracking stresses over the strain capacity of the printed specimens are 0.373, 0.382 and 0.409 for P-1L-3d, P-1L-28d, P-2L-28d, respectively; while the ratios of the cast specimens are 0.400, 0.438 and 0.585 for C-13-3d, C-13-28d, C-26-28d, respectively (Table 6). Most strain-hardening ratios are around 0.400, while the size effect of C-26-28d results in a notable reduction in both cracking stress and tensile strain capacity, leading a significant difference in strain-hardening ratio with the value of 0.585.

It should be pointed out that unlike the previous study showing an apparent improvement in tensile performance in terms of peak stress and strain capacity by using caulk-gun extrusion [46] over cast method, the improvement of the printing process on the tensile parameters is insignificant in the present printing system. In the feeding system (Fig. 1a), the mixture was transported through the hose without excessive disturbance to the mixture. In contrast, in the extruding system, the mixture would be squeezed, and fiber dispersion would be disturbed in the narrow space between the stator and rotator of the progressive cavity (PC) pump. However, during extrusion through the nozzle before placement of the printed filament, the wall effect of the printing nozzle is expected to enhance fiber alignment in the printing direction [47], which neutralizes the negative effect of the previous action and resulted in tensile property comparable to that of cast ECC specimen. In future research, therefore, more attention should be paid on the extruding system, including the use of a larger PC pump or auger pump to reduce the adverse effect on fiber dispersion of ECC.

3.4. Layer-to-layer interface fracture property of hardened 3DP-ECC

The load-displacement curves of fracture tests are summarized in Fig. 16. Although it was thought that the crack bridging effect might be

negligible due to the lack of fiber crossing the layer interface, the load-displacement curves did show a gentle rise in loading after the initial load drop, which could be attributed to the fiber-bridging effect in the smooth interface (Fig. 16a-b, d). The crack of the Inter-S-28d specimen went straight up to the loading point (Fig. 17a). It was also observed that the slopes of the second rising branches (in dashed boxes) of Intra-S-28d specimens were higher than those of Inter-S-28d specimens, indicating a stronger fiber-bridging effect in the intra-layer notched specimen.

Prior research has shown that the fracture failure mode is suppressed in ductile (cast) ECC material [48]. The fact that the load-displacement curve of Intra-S-28d shows a quasi-brittle behavior suggests that the fracture property of 3DP-ECC becomes highly anisotropic. The material becomes notch sensitive for a crack propagating in the print and fiber alignment direction.

The presence of mechanical groove-tongue interlocking (Fig. 16c) remarkably increased the load capacity after an initial drop accompanied by a tortuous crack extension (Fig. 17b). This phenomenon provided a promising method in toughening the layer interface, which could suppress any tendency of delamination failure.

The fracture toughness of inter-layer (Inter-S and Inter-G) and intra-layer (Intra-S) notched specimens with different curing ages were calculated according to RILEM specification [37] as shown in Fig. 18. All the toughness values increased with curing ages from 1d to 28d. Specifically, the fracture toughness was 0.135 and 0.252 $\text{MPa}\cdot\text{m}^{1/2}$ for Inter-S-1d and Inter-S-7d, respectively, about 50% and 95% of the value of Inter-S-28d (0.268 $\text{MPa}\cdot\text{m}^{1/2}$). The fracture toughness of Inter-G specimens shared a similar trend over curing age with a higher value of 0.322 $\text{MPa}\cdot\text{m}^{1/2}$ at 28d. The toughness values of Inter-G at all curing ages were almost equal to those of Intra-S, which indicated the potential and reliability of using the deformed interface to increase the interfacial

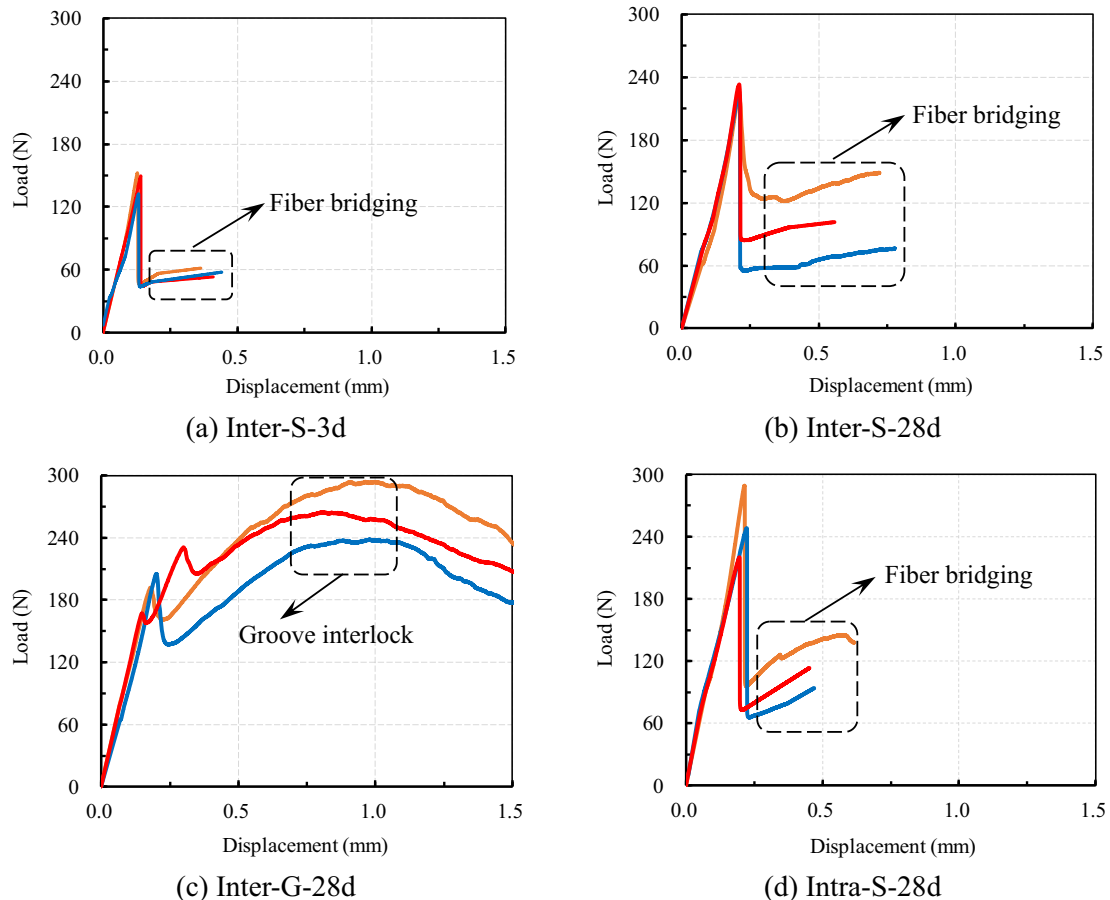


Fig. 16. Load-displacement curves of fracture test [38]



Fig. 17. Fracture behavior of three-point bending specimen [38].

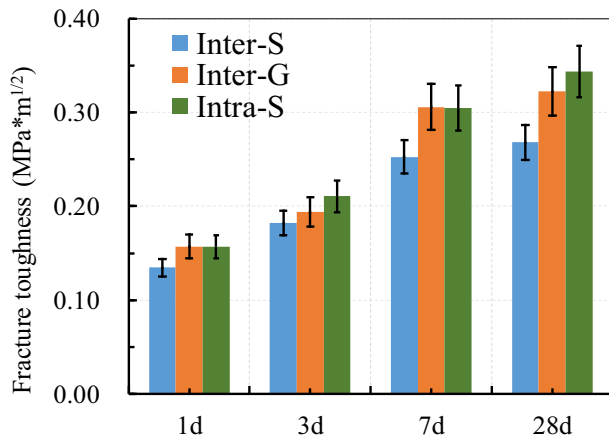


Fig. 18. Interfacial fracture toughness at different curing ages.

mechanical properties and suppress the delamination failure in the 3DP-ECC system. A further investigation of the grooved interface on the mechanical property of 3DP-ECC remains in progress.

4. Conclusions

3DP-printable engineered cementitious composite (3DP-ECC) with satisfactory flowability and buildability was developed in the present research. The developed mix was adopted in the printing of a 1.5 m tall twisted column with 150 layers using a robotic arm with customized feeding and extruding systems. The fresh behavior, including the rheological and green properties, as well as the hardened properties, including the compressive, tensile, and interfacial fracture performances of 3DP-ECC, were systematically investigated. The interactions between the print process and material properties are emphasized. Specific conclusions can be drawn as follows:

1. The flowability of 3DP-ECC was determined and optimized for the current feeding system with an open time of no more than 70 min. The developed 3DP-ECC had enough shape-retention ability and consequently buildability at 20 min after the addition of water to the dry ingredients as the start of the hydration process. The compressive stress-strain relationship obtained for green 3DP-ECC enables a deformation-based failure criterion for printed ECC elements as well as an estimation of the upper limit of print speed.
2. The compressive strengths of hardened 3DP-ECC specimens increased with curing ages from 1d to 28d. Anisotropic (perpendicular versus parallel to the layer interface) behavior was found. The Prism-Per specimen exhibited a more ductile failure mode accompanied by higher compressive strength and corresponding strain, and a gentler descending branch compared to those of Prism-Par specimens. However, due to the closing of the space at layer interfaces, the

Young's modulus of Prism-Per specimen was 16% lower than that of Prism-Par prism, which could induce a larger deformation of 3DP-ECC element and require special attention in the future design of 3DP structural elements.

3. Under uniaxial tension, the 3DP-ECC demonstrated robust multiple microcracking and strain-hardening performance with a strain capacity of 3.0%. The tensile properties exhibited a negligible size effect due to the consistent fiber orientation in both 1- and 2-layer specimens.
4. For printed smooth interface, a slight fiber-bridging effect was found in fracture specimens, contributing to a gentle rise in the load-displacement curve after an initial drop when a crack extends along with the interface from the notch tip. This unexpected effect is likely due to fiber interpenetration across the deposited layers in the green state. However, the interface remains quasi-brittle. With deliberate print grooving using a shaped nozzle, mechanical interlock between the printed filaments was found to introduce a non-brittle failure response with remarkably higher loading capacity. Groove-printing appears to be a promising approach towards toughening the filament-to-filament interface for suppression of delamination failure tendency in 3DP-ECC structures.

The present pilot study on the fresh rheological properties and hardened mechanical properties of 3DP-ECC establishes the foundation of 3D printing of self-reinforcing strain-hardening ECC. Further investigations, however, are needed. These include the improvement of the tensile property of printed ECC by either reducing the negative influence of the PC pump and/or increasing the positive wall effect of the extruding nozzle. A more direct characterization of fiber dispersion and orientation in extruded filaments should also be conducted in future studies.

Declaration of competing interest

The authors declare that there's no financial/personal interest or belief that could affect their objectivity. The authors confirm explicitly that no conflicts of interest exist.

Acknowledgment

Financial support of this research is provided by the Department of Civil and Environmental Engineering, the College of Engineering, the Taubman College of Architecture and Urban Planning's Prototyping Tomorrow Grant Initiative, and the University of Michigan MCubed 3.0, as well as the Clusters and Theme programs. A faculty fellow gift from the Jiangsu Industrial Technology Research Institute (JITRI) on robotic additive research is also acknowledged.

CRediT authorship contribution statement

K Yu: Investigation, Data Curation, Writing - Original Draft. W.

McGee, T.Y. Ng: Data Curation, Supervision, Writing - Review & Editing. **H. Zhu:** Data Curation, Writing - Review & Editing. **VC Li:** Conceptualization, Supervision, Funding Acquisition, Resources, Writing - Review & Editing.

References

- [1] B. Khoshnevis, R. Dutton, Innovative rapid prototyping process makes large sized, smooth surfaced complex shapes in a wide variety of materials, *Mater. Technol.* 13 (1998) 53–56.
- [2] P. Wu, J. Wang, X. Wang, A critical review of the use of 3-D printing in the construction industry, *Automat. Constr.* 68 (2016) 21–31.
- [3] T. Wangler, N. Roussel, F.P. Bos, T.A. Salet, R.J. Flatt, Digital concrete: a review, *Cem. Concr. Res.* 123 (2019) 105780.
- [4] G. Ma, L. Wang, Y. Ju, State-of-the-art of 3D printing technology of cementitious material—an emerging technique for construction, *Sci. China Technol. Sci.* 61 (2018) 475–495.
- [5] Y. Liu, S. Nederveen, M. Hertogh, Understanding effects of BIM on collaborative design and construction: an empirical study in China, *Int. J. Proj. Manag.* 35 (2017) 686–698.
- [6] S. Lim, R.A. Buswell, T.T. Le, S.A. Austin, A.G. Gibb, T. Thorpe, Developments in construction-scale additive manufacturing processes, *Automat. Constr.* 21 (2012) 262–268.
- [7] C. Gosselin, R. Duballet, P. Roux, N. Gaudillière, J. Dirrenberger, P. Morel, Large-scale 3D printing of ultra-high performance concrete—a new processing route for architects and builders, *Mater. Design.* 100 (2016) 102–109.
- [8] G.D. Schutter, K. Lesage, V. Mechtcherine, V.N. Nerella, G. Habert, I. Agusti-Juan, Vision of 3D printing with concrete—technical, economic and environmental potentials, *Cem. Concr. Res.* 112 (2018) 25–36.
- [9] W.F. Chen, J.Y.R. Liew, *The Civil Engineering Hand Book*, 2nd ed., CRC Press LLC, New York, 2003.
- [10] D. Asprone, C. Menna, F.P. Bos, T.A. Salet, J. Mata-Falcón, W. Kaufmann, Rethinking reinforcement for digital fabrication with concrete, *Cem. Concr. Res.* 112 (2018) 111–121.
- [11] V. Mechtcherine, A. Michel, M. Liebscher, Schneider, K., C. Großmann, Mineral-impregnated carbon fiber composites as novel reinforcement for concrete construction: Material and automation perspectives, *Automat. Constr.* 110 (2020) 103002.
- [12] V. Mechtcherine, J. Grafe, V.N. Nerella, E. Spaniol, M. Hertel, U. Füssel, 3D-printed steel reinforcement for digital concrete construction—manufacture, mechanical properties and bond behaviour, *Constr. Build. Mater.* 179 (2018) 125–137.
- [13] Z. Li, L. Wang, G. Ma, Mechanical improvement of continuous steel microcable reinforced geopolymer composites for 3D printing subjected to different loading conditions, *Compos. Part B- Eng.* 187 (2020) 107796.
- [14] V.C. Li, *Engineered Cementitious Composites (ECC)*, Springer, 2019.
- [15] K. Yu, L. Li, J. Yu, Y. Wang, J. Ye, Q. Xu, Direct tensile properties of engineered cementitious composites: a review, *Constr. Build. Mater.* 165 (2018) 346–362.
- [16] Y. Bao, M. Xu, D. Soltan, T. Xia, A. Shih, H.L. Clack, V.C. Li, Three-dimensional printing multifunctional engineered cementitious composites (ECC) for structural elements, in: *RILEM International Conference on Concrete and Digital Fabrication*, Springer, Cham, 2018, pp. 115–128.
- [17] K. Yu, L. Li, J. Yu, J. Xiao, J. Ye, Y. Wang, Feasibility of using ultra-high ductility cementitious composites for concrete structures without steel rebar, *Eng. Struct.* 170 (2018) 11–20.
- [18] R. Zhu, J. Pan, B. Nematollahi, Z. Zhou, Y. Zhang, J. Sanjayan, Development of 3D printable engineered cementitious composites with ultra-high tensile ductility for digital construction, *Mater. Design.* 181 (2019) 108088.
- [19] H. Ogura, V. Nerella, V. Mechtcherine, Developing and testing of strain-hardening cement-based composites (SHCC) in the context of 3D-printing, *Materials.* 11 (2018) 1375.
- [20] S.C. Figueiredo, C.R. Rodríguez, Z.Y. Ahmed, D.H. Bos, Y. Xu, T.M. Salet, F.P. Bos, An approach to develop printable strain hardening cementitious composites, *Mater. Design.* 169 (2019) 107651.
- [21] B. Zareiyan, B. Khoshnevis, Effects of interlocking on interlayer adhesion and strength of structures in 3D printing of concrete, *Automat. Constr.* 83 (2017) 212–221.
- [22] J.G. Sanjayan, B. Nematollahi, M. Xia, T. Marchment, Effect of surface moisture on inter-layer strength of 3D printed concrete, *Constr. Build. Mater.* 172 (2018) 468–475.
- [23] V.N. Nerella, S. Hempel, V. Mechtcherine, Effects of layer-interface properties on mechanical performance of concrete elements produced by extrusion-based 3D-printing, *Constr. Build. Mater.* 205 (2019) 586–601.
- [24] S.C. Paul, Y.W.D. Tay, B. Panda, M.J. Tan, Fresh and hardened properties of 3D printable cementitious materials for building and construction, *Arch. Civ. Mech. Eng.* 18 (2018) 311–319.
- [25] R.J.M. Wolfs, F.P. Bos, T.A.M. Salet, Hardened properties of 3D printed concrete: the influence of process parameters on interlayer adhesion, *Cem. Concr. Res.* 119 (2019) 132–140.
- [26] G. Ma, Z. Li, L. Wang, F. Wang, J. Sanjayan, Mechanical anisotropy of aligned fiber reinforced composite for extrusion-based 3D printing, *Constr. Build. Mater.* 202 (2019) 770–783.
- [27] W. McGee, T.Y. Ng, K. Yu, V.C. Li, Extrusion nozzle shaping for improved 3DP of engineered cementitious composites (ECC/SHCC), in: *RILEM International Conference on Concrete and Digital Fabrication*, Springer, Cham, 2020, July, pp. 916–925.
- [28] R.A. Buswell, W.L. de Silva, S.Z. Jones, J. Dirrenberger, 3D printing using concrete extrusion: a roadmap for research, *Cem. Concr. Res.* 112 (2018) 37–49.
- [29] V. Mechtcherine, V.N. Nerella, K. Kasten, Testing pumpability of concrete using sliding pipe rheometer, *Constr. Build. Mater.* 53 (2014) 312–323.
- [30] A. Perrot, D. Rängeard, A. Pierre, Structural built-up of cement-based materials used for 3D-printing extrusion techniques, *Mater. Struct.* 49 (2016) 1213–1220.
- [31] A. Kazemian, X. Yuan, E. Cochran, B. Khoshnevis, Cementitious materials for construction scale 3D printing: laboratory testing of fresh printing mixture, *Constr. Build. Mater.* 145 (2017) 639–647.
- [32] ASTM C1437, *Standard test method for flow of hydraulic cement mortar.*
- [33] B. Nematollahi, P. Vijay, J. Sanjayan, A. Nazari, M. Xia, V. Naidu Nerella, V. Mechtcherine, Effect of polypropylene fibre addition on properties of geopolymers made by 3D printing for digital construction, *Materials.* 11 (2018) 2352.
- [34] J.D. Helm, Digital image correlation for specimens with multiple growing cracks, *Exp. Mech.* 48 (6) (2008) 753–762.
- [35] T.C. Chu, W.F. Ranson, M.A. Sutton, Applications of digital-image-correlation techniques to experimental mechanics, *Exp. Mech.* 25 (3) (1985) 232–244.
- [36] JSCE, *Recommendations for Design and Construction of High Performance Fiber Reinforced Cement Composites with Multiple Fine Cracks*, Japan Society of Civil Engineers, Tokyo, Japan, pp. 1–16.
- [37] S.P. Shah, Determination of fracture parameters (K_{Ic} and $CTOD_c$) of plain concrete using three-point bend tests, *Mater. Struct.* 23 (1990) 457–460.
- [38] V.C. Li, F.P. Bos, K. Yu, W. McGee, T.Y. Ng, S.C. Figueiredo, G.P. van Zijl, On the emergence of 3D printable engineered, strain hardening cementitious composites (ECC/SHCC), *Cem. Concr. Res.* 132 (2020) 106038.
- [40] B. Panda, J.H. Lim, M.J. Tan, Mechanical properties and deformation behaviour of early age concrete in the context of digital construction, *Compos. Part B-Eng.* 165 (2019) 563–571.
- [41] K. Yu, Y. Wang, J. Yu, S. Xu, A strain-hardening cementitious composites with the tensile capacity up to 8%, *Constr. Build. Mater.* 137 (2017) 410–419.
- [42] V.C. Li, High performance fiber reinforced cementitious composites as durable material for concrete structure repair, *Int. J. Restor.* 10 (2004) 163–180.
- [43] Y. Ding, K. Yu, W. Mao, Compressive performance of all-grade engineered cementitious composites: experiment and theoretical model, *Constr. Build. Mater.* 244 (2020) 118357.
- [44] J. Zhou, J. Pan, C.K. Leung, Mechanical behavior of fiber-reinforced engineered cementitious composites in uniaxial compression, *J. Mater. Civil. Eng.* 27 (2015), 04014111.
- [45] V.C. Li, S. Wang, On high performance fiber reinforced cementitious composites, *Proceeding of the JCI Symposium on Ductile Fiber Reinforced Cementitious Composites (DFRCC)*, Tokyo, Japan, pp. 13–23, 2003.
- [46] D.G. Soltan, V.C. Li, A self-reinforced cementitious composite for building-scale 3D printing, *Cem. Concr. Compos.* 90 (2018) 1–13.
- [47] F. Laranjeira, A. Aguado, C. Molins, S. Grünwald, J. Walraven, S. Cavalaro, Framework to predict the orientation of fibers in FRC: a novel philosophy, *Cem. Concr. Res.* 42 (2012) 752–768.
- [48] M. Maalej, T. Hashida, V.C. Li, Effect of fiber volume fraction on the off-crack-plane fracture energy in strain-hardening engineered cementitious composites, *J. Am. Ceram. Soc.* 78 (1995) 3369–3375.